Supporting Information

Valence-variable thiospinels for ampere-scale water electrolysis

Shuowen Bo,[a,#] Fumin Tang,[b,#] Hui Su,[a,*] Xiuxiu Zhang,[a] Feifan Yu,[c] Wanlin Zhou,[a] Meihuan Liu,[a] Weiren Cheng,[a] Juguang Han,[a] and Qinghua Liu[a,*]

[a] *National Synchrotron Radiation Laboratory, University of Science and Technology of China, Hefei 230029, Anhui, P. R. China*

[b] *School of Automotive Studies & Clean Energy Automotive Engineering Center, Tongji University (Jiading Campus), 4800 Caoan Road, Shanghai, 201804, China*

[c] *School of Chemistry and Chemical Engineering, Key Laboratory for Green Processing of Chemical Engineering of Xinjiang Bingtuan, Shihezi University, Shihezi 832003, China*

*E-mail: suhui@ustc.edu.cn; qhliu@ustc.edu.cn

Contents:

Materials and methods;

Supplementary Figs 1-23;

Supplementary Tables 1-4;

Materials and methods

Materials. $Cu(NO_3)_2·3H_2O$, $Co(NO_3)_2·6H_2O$, $Co(NH_2)_2$, $Mn(NO_3)_2·4H_2O$, VCl_4, $Cr(NO_3)_3·9H_2O$, NH_4F, $Na_2S·9H_2O$, KOH, ethanol, acetone, hydrochloric acid were purchased from Sinopharm Chemical Reagent Co, Ltd. Commercial RuO_2 was purchased from Aladdin. All chemicals were used directly without further purification. Deionized water was used in all experiments.

Synthesis of Mn-$CuCo_2S_4$/NFelectrocatalyst. The Mn-$CuCo_2S_4$ electrocatalysts was fabricated in four convenience designed steps, consisting of surface functionalization of 3D nickel foam (NF), high temperature hydrothermal precursors synthesis, hydrothermal vulcanization synthesis, and room temperature-conventional drying. First, the 3D nickel foam was cleaned by ultrasound vibration at 60 °C for 4 h, then nickel foam was washed with concentrated nitric and deionized water. Next, chemical ratios of Cu $(NO_3)_2·3H_2O$, $Co(NO_3)_2·6H_2O$, $Co(NH_2)_2$, traces of $Mn(NO_3)_2·4H_2O$, and NH_4F were mixed in 70 ml deionized water for 10 minutes, and the nickel foam and solution were put into a 45 ml polytetrafluoroethylene reactor, and the resulting mixed solution was dried at 120 °C for 8 h to obtain solid precursor, then the precursor was washed with deionized water and ethanol for 3 times. Next, the precursor was dried in a vacuum oven at 60 °C for 6 h. Subsequently, 0.05 mol of $Na_2S·9H_2O$ was dissolved into 40 ml deionized water to form the solution, then the nickel foam was put in the solution. The resulting solution was put into a 45 ml polytetrafluoroethylene reactor. The resulting solution was heated at 110 °C for 4 h, then washed three times with deionized water and ethanol. Finally, the resulting product was wiped with lint-free paper, then cooled at room temperature until dry naturally.

Synthesis of V-$CuCo_2S_4$/NF electrocatalyst. The general process of synthesis is similar to the preparation of Mn-$CuCo_2S_4$/NF electrocatalyst. It is noted that in the

process of high temperature hydrothermal precursors synthesis, the metal salt was replaced with VCl_4, and the final catalyst is called V-$CuCo_2S_4$/NFelectrocatalyst.

Synthesis of Cr-$CuCo_2S_4$/NF electrocatalyst. The general process of synthesis is similar to the preparation of Mn-$CuCo_2S_4$ electrocatalyst. It is noted that in the process of high temperature hydrothermal precursors synthesis, the metal salt was replaced with $Cr(NO_3)_3 \cdot 9H_2O$, and the final catalyst is called Cr-$CuCo_2S_4$/NF electrocatalyst.

Synthesis of $CuCo_2S_4$/NF electrocatalyst. The general process of synthesis is similar to the preparation of Mn-$CuCo_2S_4$ electrocatalyst without the addition of other metal salts, and the final catalyst is called $CuCo_2S_4$/NF electrocatalyst.

Morphology and structure characterizations.

The powder X-ray diffraction (XRD) patterns of samples were measured in a Philips X' Pert Pro Super X-ray diffractometer with Cu Kα radiation (λ = 1.54178 Å). Transmission electron microscopy (TEM), high-resolution transmission electron microscopy (HRTEM) and energy dispersive spectroscopy (EDS) were performed on a JEM-2100F microscope with an acceleration voltage of 200 kV. The field emission scanning electron microscopy (SEM) was acquired on a Gemini SEM 500 scanning electron microscope. X-ray photoelectron spectroscopy (XPS) spectra were acquired on an ESCALAB MKII with Mg Kα (hυ = 1253.6 eV) as the excitation source. The Co K-edge X-ray absorption near-edge spectra (XANES) were measured in National Synchrotron Radiation Laboratory (NSRL), which were measured in the total electron yield mode in a vacuum chamber (< 5×10^{-8} Pa). Inductively coupled plasma mass spectrometry (ICP-OES) was measured by using Inductively Coupled Plasma Optic Emission Spectrometer (Plasma Quad 3). Specific surface area (BET) was measured in a fully automatic surface area and porosity analyzer (Tristar II 3020M)

Electrochemical Measurements. All electrochemical measurements were performance in a three-electrode system by CHI760D electrochemical work station,

operated with the self-supporting array grown on NF (the active area of 1×1 cm^{-2}) as the working electrodes, platinum net as the counter electrode, and the normal Hg/Hg_2Cl_2 electrode as the reference electrode. The three electrodes were immersed in 1M KOH as conductive media. All final potentials were converted to reversible hydrogen electrode (RHE) with the conversion E (vs. RHE) = E (vs. Hg/Hg_2Cl_2) + 0.245 V + 0.059 × PH. Linear sweep voltammetry (LSV) curves were obtained at a rate of 5 mV s^{-1} with IR correction after several cyclic voltammetry tests until stable. It is worth noting that electrochemical data were corrected for uncompensated series resistance R_s, which was determined through the open-circuit voltage, and we selected 90% IR compensation to obtain R_s. And the potential was determined by the following Eq: $E_{Corrected} = E_{Uncorrected} - I*R_S$

Mathematical formula for electrochemical measurements:

The roughness factor (RF) mathematical formula. The roughness factor (RF) was calculated by taking the estimated ECSA and S_{geo}, as following Eq.

$$RF=ECSA/ S_{geo}$$

The ECSA mathematical formula. The ECSA of the catalyst sample was calculated from the double layer capacitance according to the following Eq.

$$ECSA = C_{dl} / C_s$$

where C_s is the specific capacitance of the sample, and the typical value reported ranges between Cs= 0.02-0.06 mF/cm^2 in KOH, then we selected general specific capacitances of Cs=0.04 mF/cm^2.

based typical reported. Furthermore, to gain reliable data, we performed CV tests at a wide redox process-free window of 300 mV and suitable sweep speeds of 0.005, 0.01, 0.02, 0.05, 0.1, 0.5, 0.8, 1 V/s.

The J_{ECSA} mathematical formula. The definition of specific activity refers to the specific current density J_{ECSA}, which was calculated as according to the following Eq.

$$J_{ECSA} = J_{geo} /RF$$

The turnover frequency (TOF) and mass activity mathematical formula.

$$TOF = \frac{the\ measured\ current\ density\ j * NA * 1000}{4 * F * mol}$$

$$MA\ (mass\ activity) = \frac{j}{m}$$

The TOF and MA are activity metric reported in the electrocatalysis literature, which are depended on a given overpotential and the measured current density.

***In-situ* XAFS measurements.**

The *in-situ* XAFS measurements of Co *K*-edge were carried out at the 1W1B station in the Beijing Synchrotron Radiation Facility (BSRF), China. The storage ring of BSRF was operated at 2.5 GeV with a maximum current of 250 mA. The beam from the bending magnet was monochromatized utilizing a Si (111) double-crystal monochromator. The data collection was carried out in transmission mode using ionization chamber for Co foil, and in fluorescence excitation mode for Mn-$CuCo_2S_4$/NF. *In-situ* XAFS measurements were performed with M-$CuCo_2S_4$/NF catalyst-coated carbon cloths in 1 M KOH solution by a smart homemade cell, and the XAFS spectra were collected through fluorescence mode. The Mn-$CuCo_2S_4$/NF electrocatalyst on carbon cloths was cut into 1*2 cm^2 pieces and then sealed in a cell by Kapton film. To obtain the evolution information of the active site during the electrochemical reaction, a series of representative potentials (1.2–1.55 V) were applied to the electrode.

XAFS data analysis. To obtain the detailed structural parameters around Co atoms in the samples, the EXAFS data were processed according to the standard procedures using the ATHENA and ARTEMIS module implemented in the IFEFFIT software packages. The k^3-weighted $\chi(k)$ data in the k-space were Fourier-transformed to real R-space using hanning windows (dk = 1.0 $Å^{-1}$). For the fitting of Co K-edge data, the amplitude reduction factor S_0^2 was treated as adjustable variable and the obtained value of 0.77 for Co foil, which was fixed in fitting the subsequent Co K-edge data for Mn-$CuCo_2S_4$ /NF. The Co–O, Co–S and Co–Co scattering paths were considered to fit the

EXAFS data. For the fitting of Mn-$CuCo_2S_4$/NF under OER operation, the fit was done on the k^3-weighted EXAFS function $\chi(k)$ data from 2.3 to 11.5 $Å^{-1}$ in the R-range of 1.0–3.0 Å. The coordination numbers N, interatomic distances R, Debye-Waller factor σ^2 and the edge-energy shift ΔE_0 were allowed to run freely.

***In-situ* SRIR measurement.**

In-situ synchrotron radiation IR measurements were made at the infrared beamline BL01B of the National Synchrotron Radiation Laboratory (NSRL, China), and we performed electrochemical tests through a homemade top-plate cell to obtain better signal data. Specifically, in order to reduce the loss of infrared light and eliminate the effect of vibration absorption of water molecules, the catalyst electrode was tightly pressed against the ZnSe crystal window with a micron-scale gap. Attentively, during the *in-situ* SRIR measurements, the infrared signal is very sensitive to water molecules and it is easily disturbed. To obtain improved-infrared signal-to-noise ratio (SNR), we pressed the electrode and window to control the thickness of the water film on the micron scale. To avoid signal differences caused by sample shedding, infrared spectra were collected after a constant potential was applied to the catalyst electrode for 5 min. Before each systemic OER measurement, the background spectrum of the electrocatalyst electrode was acquired without applied voltage and the measure potential ranges of the OER were 1.2–1.6 V with an interval of 0.1 V.

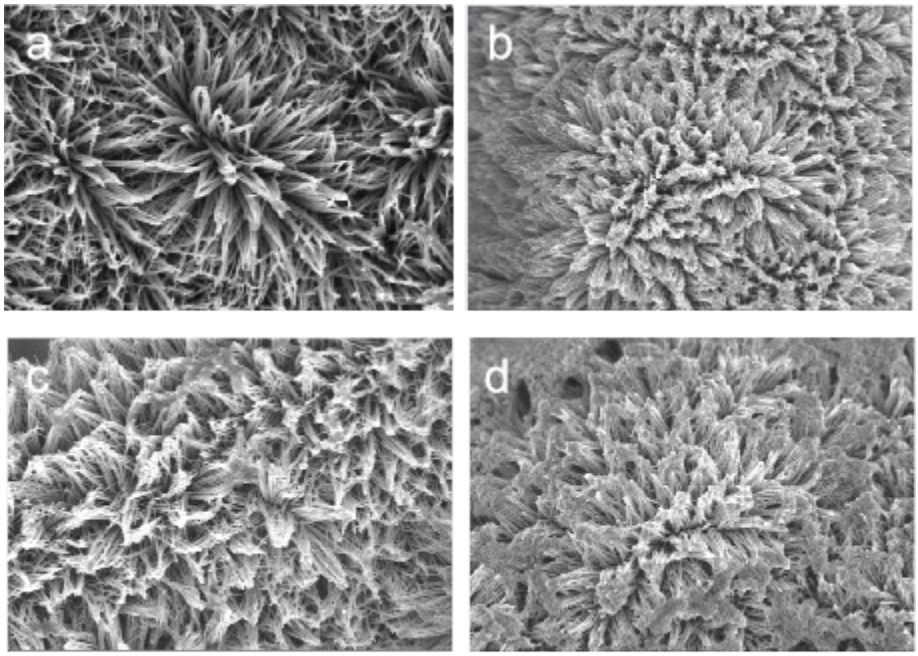

Figure S1. SEM images of $CuCo_2S_4$ /NF(a) and M-$CuCo_2S_4$ /NF(b,c,d)

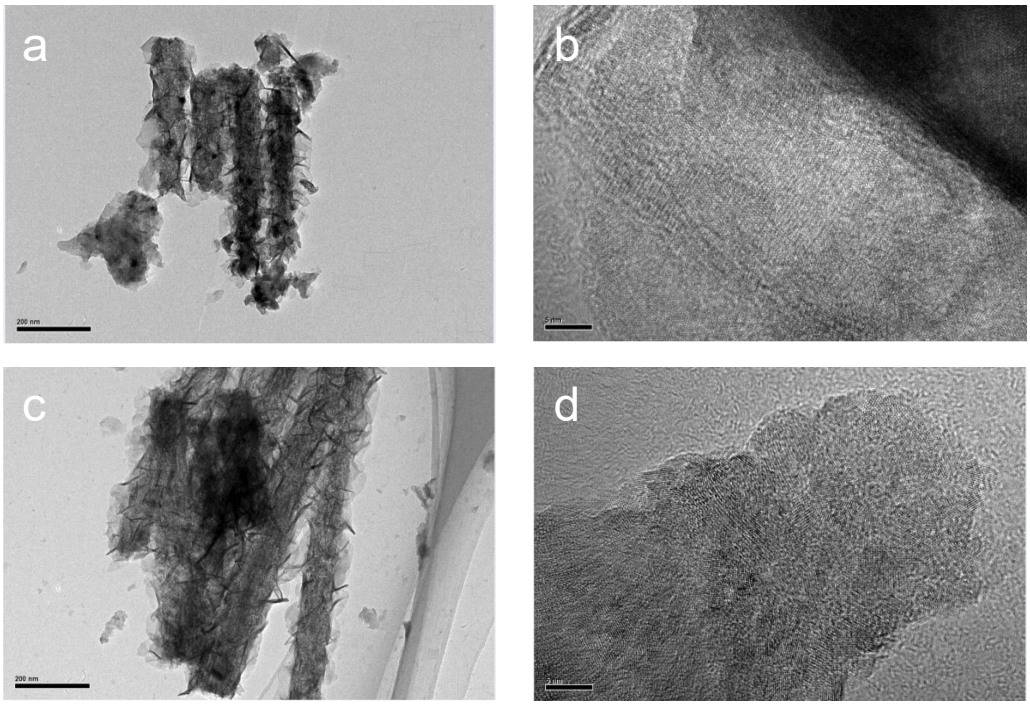

Figure S2. TEM images of $CuCo_2S_4$/NF (a) and Mn-$CuCo_2S_4$/NF(c) HRTEM images of $CuCo_2S_4$ /NF(b) and Mn-$CuCo_2S_4$ /NF(d)

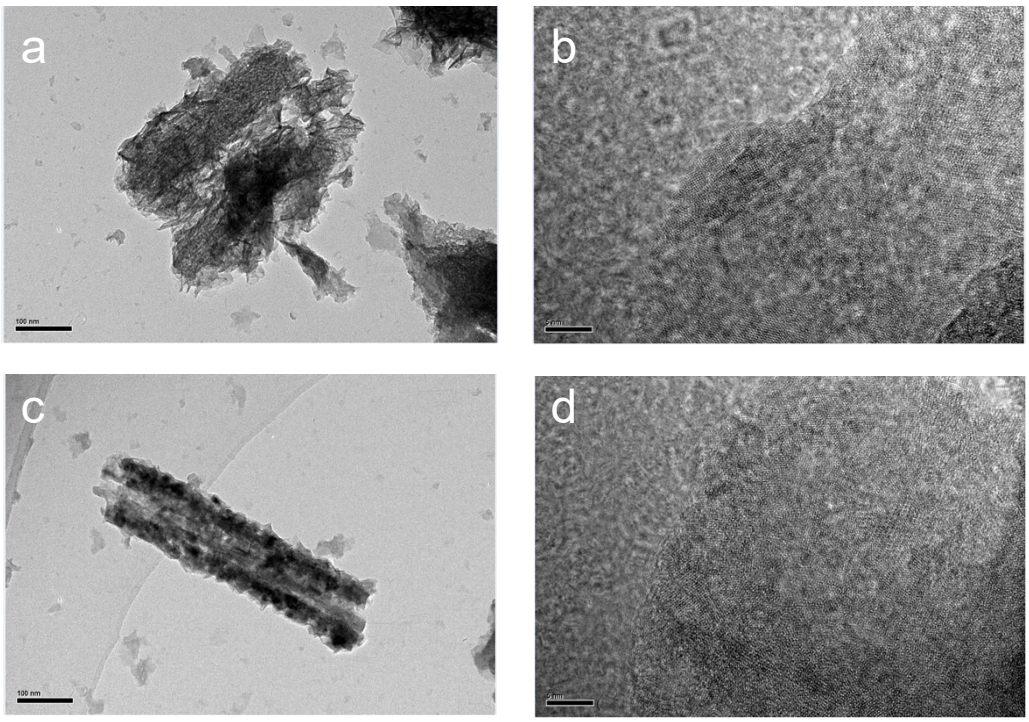

Figure S3. TEM images of V-$CuCo_2S_4$/NF(a) and Cr-$CuCo_2S_4$/NF(c) HRTEM images of V-$CuCo_2S_4$/NF(b) and Cr-$CuCo_2S_4$/NF(d)

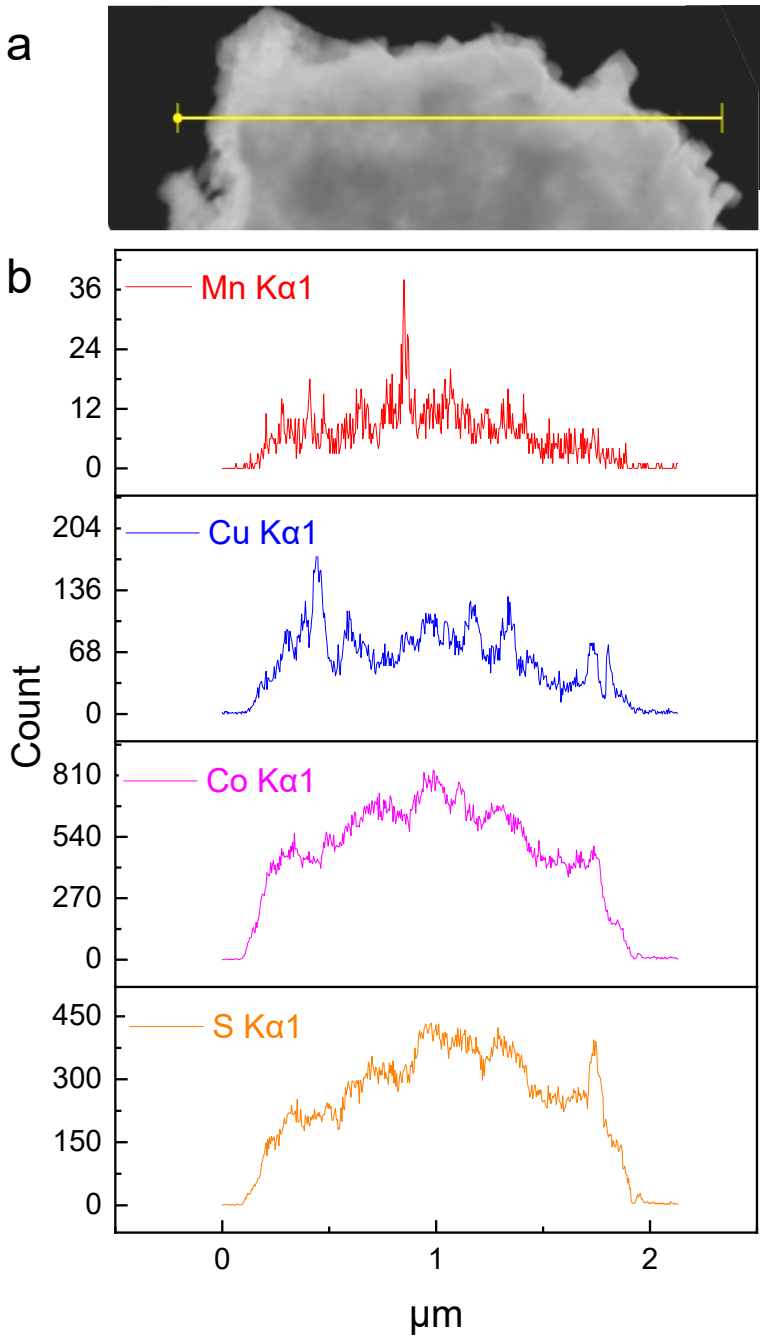

Figure S4. Linear scan content distribution of Mn-$CuCo_2S_4$/NF

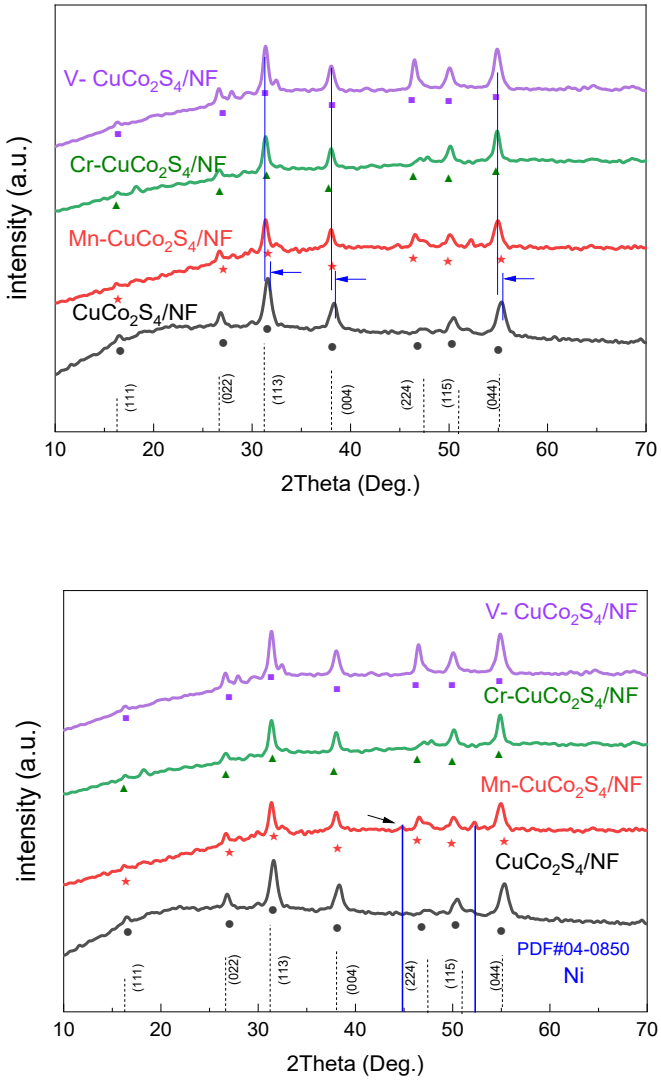

Figure S5. XRD diffraction pattern of M-$CuCo_2S_4$/NF(M=Mn, Cr, V)

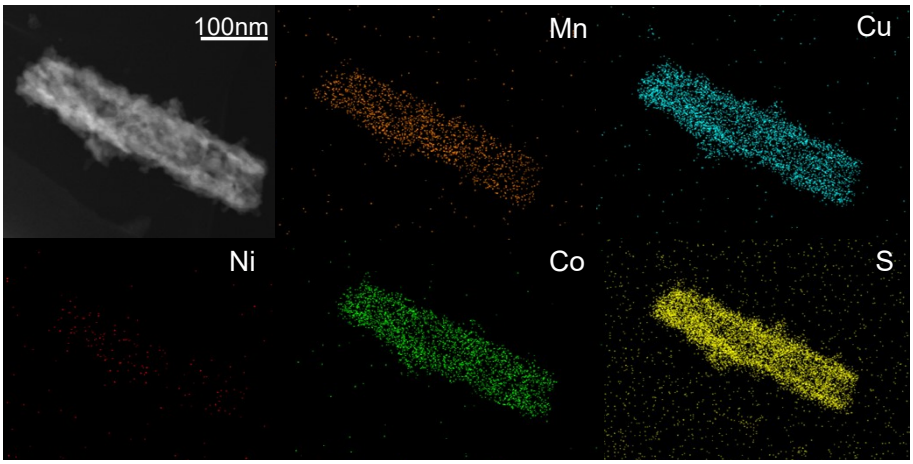

Figure S6. TEM-EDX images of Mn-$CuCo_2S_4$/NF

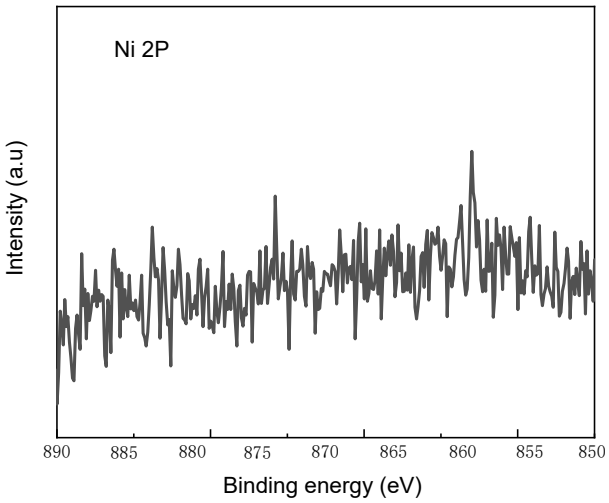

Figure S7. XPS survey spectra of Ni.

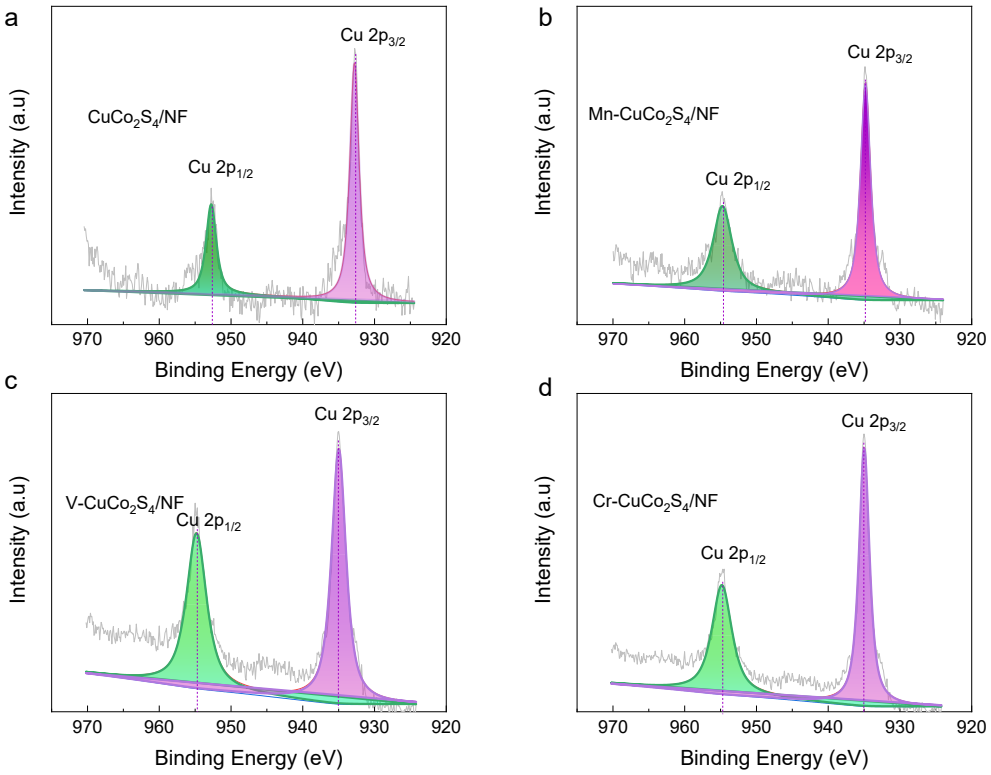

Figure S8. The Cu 2p XPS survey spectra of M-$CuCo_2S_4$/NFelectrocatalysts

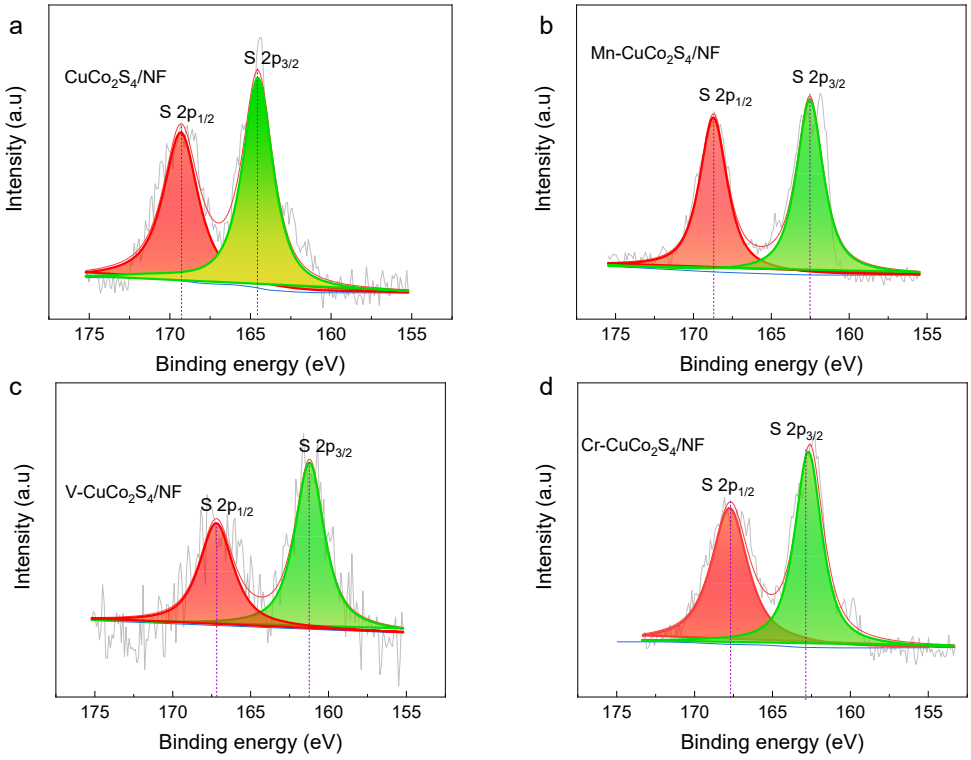

Figure S9. The S 2p XPS survey spectra of M-$CuCo_2S_4$/NF electrocatalysts

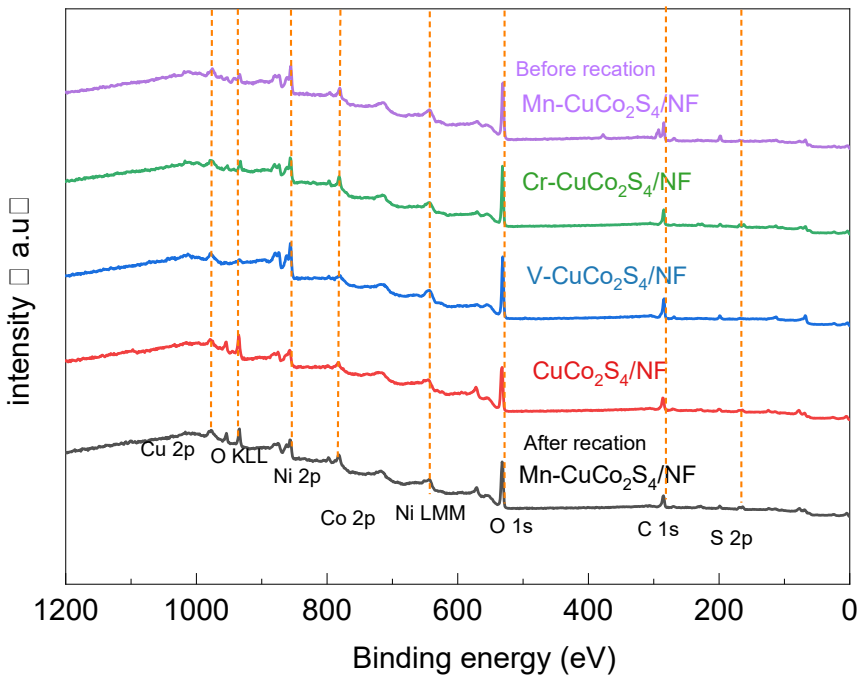

Figure S10. XPS survey spectra of M-$CuCo_2S_4$/NFelectrocatalyst

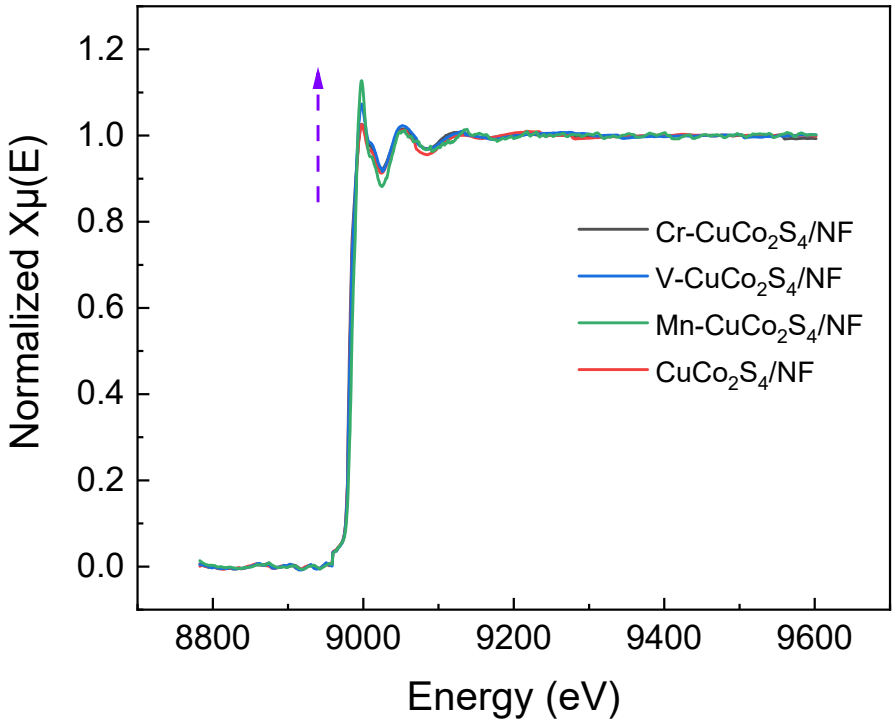

Figure S11. The Cu *K*-edge XANES spectra of *v*-M-$CuCo_2S_4$/NF (v-M = Mn, V, and Cr) and $CuCo_2S_4$/NF.

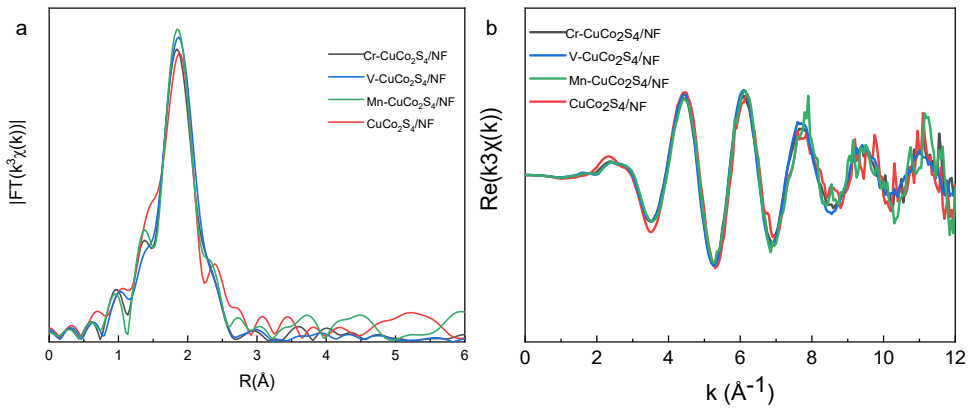

Figure S12. The Cu *K*-edge EXAFS spectra Fourier transform (FT) spectra and Re($k_3\chi$(k)) oscillation curves for *v*-M-$CuCo_2S_4$/NF (v-M = Mn, V, and Cr) and $CuCo_2S_4$/NF.

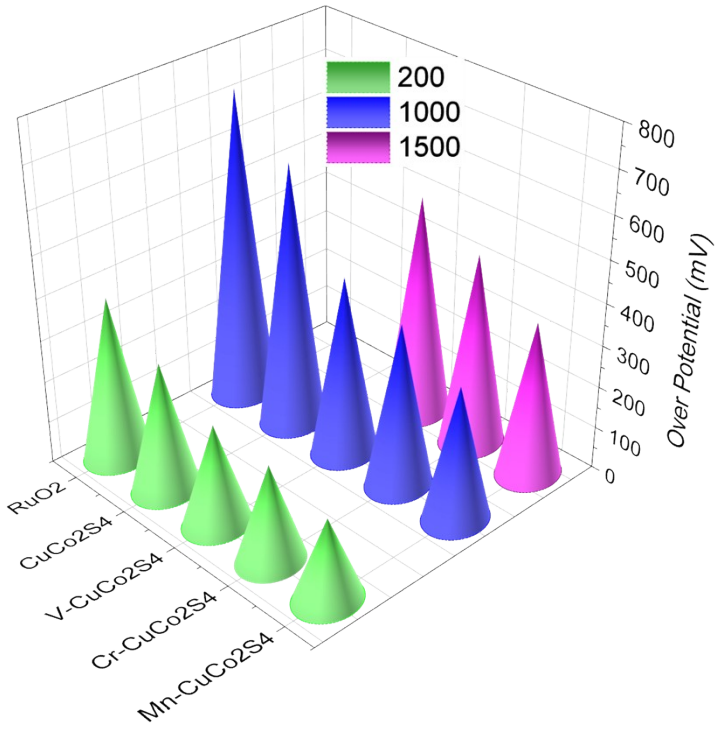

Figure S13. Stereoscopic diagram of overpotential in M-$CuCo_2S_4$/NF

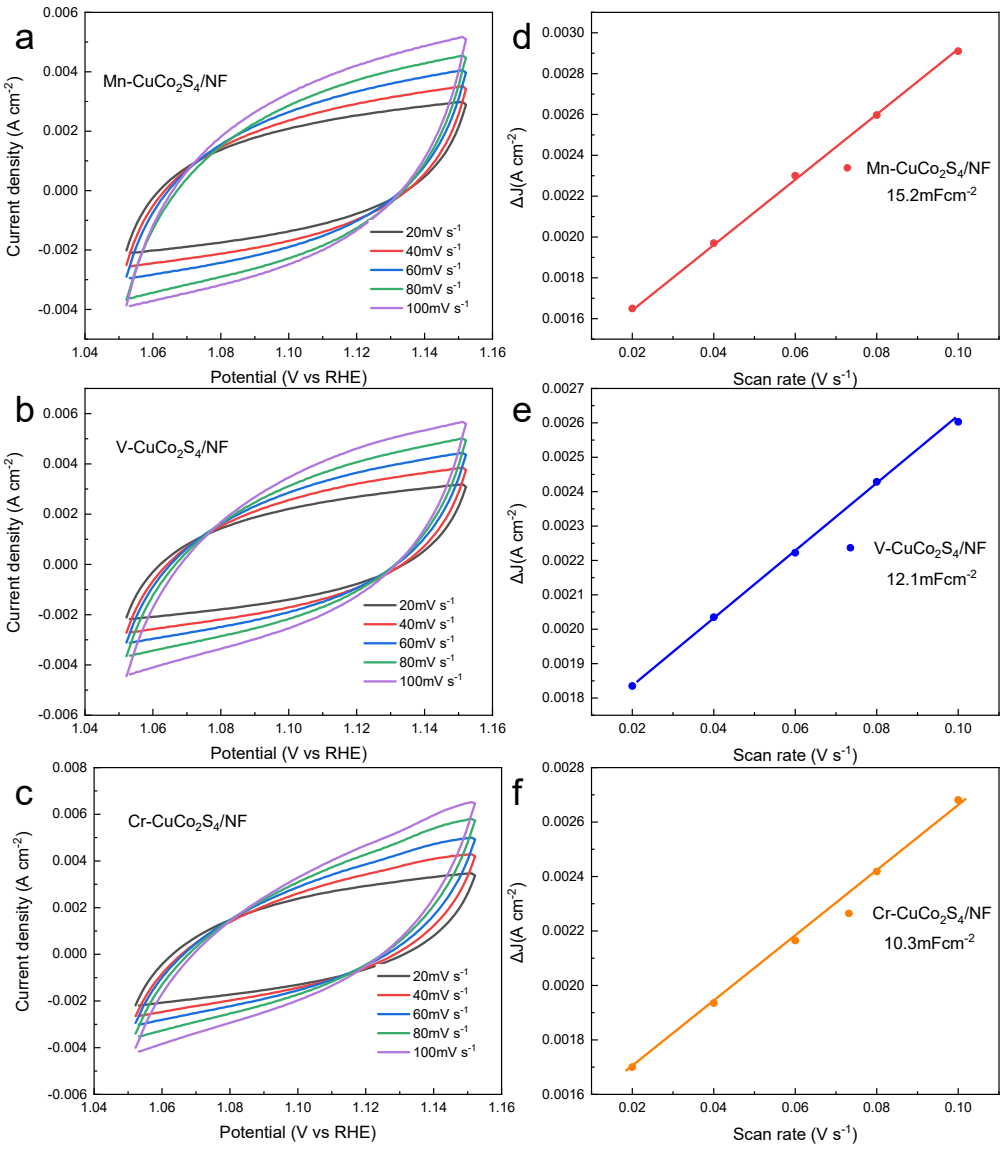

Figure S14. Double-layer capacitance (C_{dl}) measurements. (a), (b) and (c) CVs were conducted in a non-Faradaic region at the following scan rate: 20, 40, 60, 80, 100 mV s^{-1}. (d), (e) and (f) The difference in charging currents variation at a potential plotted against scan rate for estimation of double-layer capacitance.

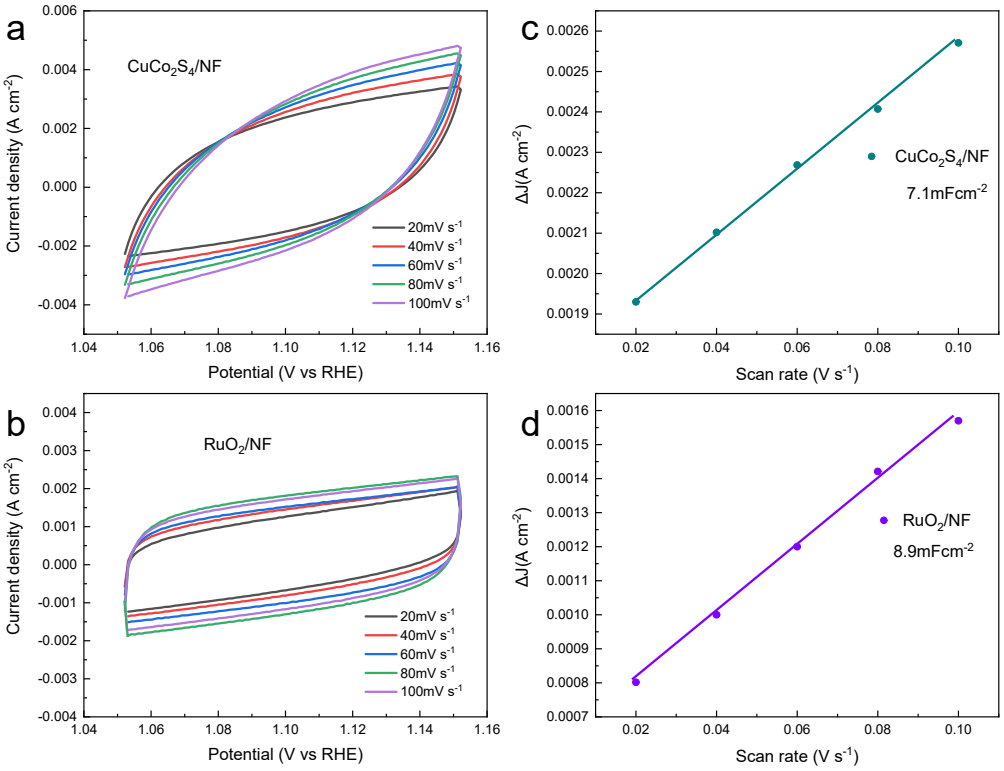

Figure S15. Double-layer capacitance (C_{dl}) measurements. (a) and (b) CVs were conducted in a non-Faradaic region at the following scan rate: 20, 40, 60, 80, 100 mV s^{-1}. (c) and (d) The difference in charging currents variation at a potential plotted against scan rate for estimation of double-layer capacitance.

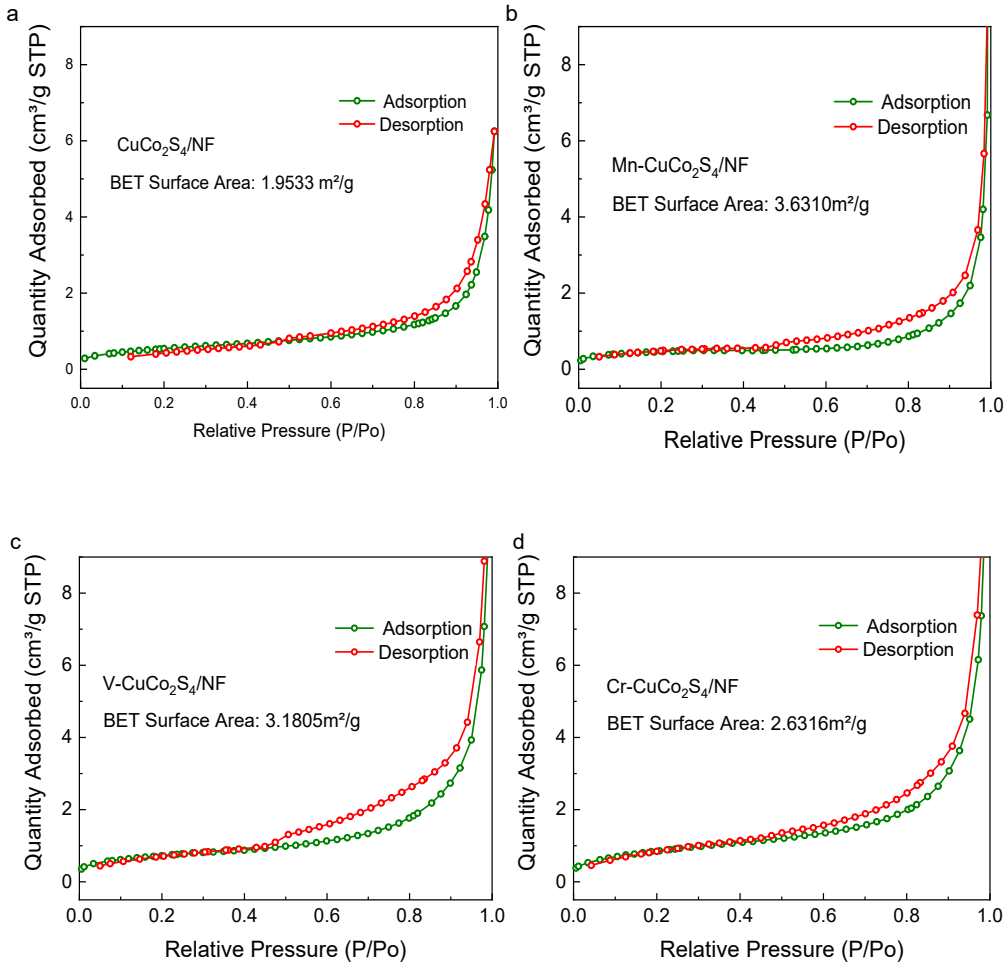

Figure S16. Isotherm adsorption curve and specific surface area of M-$CuCo_2S_4$/NF

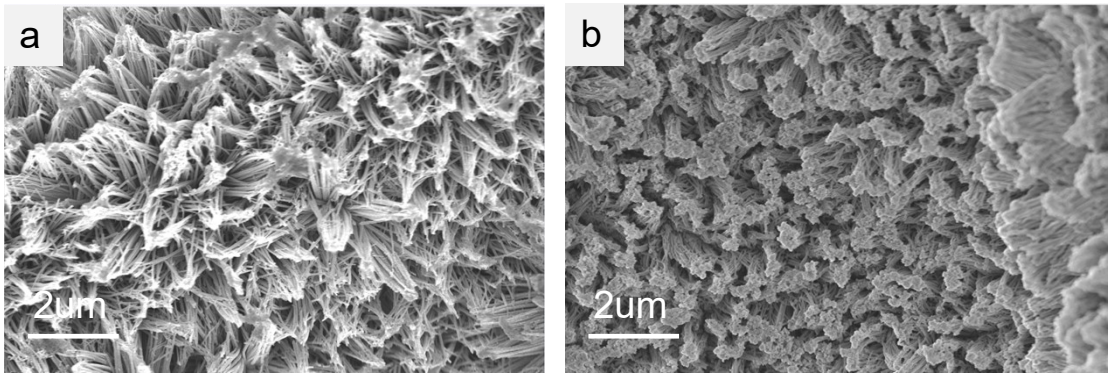

Figure S17. SEM images for Mn-$CuCo_2S_4$/NF electrocatalyst before (a) and after (b) electrochemical measurements.

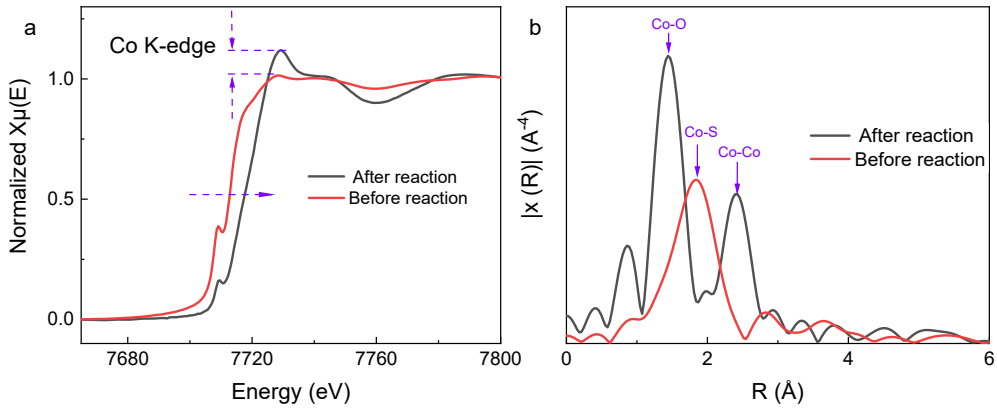

Figure S18. (a) The Co *K*-edge XANES spectra and (b) the Co *K*-edge k^3-weighted EXAFS profiles of Mn-$CuCo_2S_4$/NF before and after electrochemical measurements

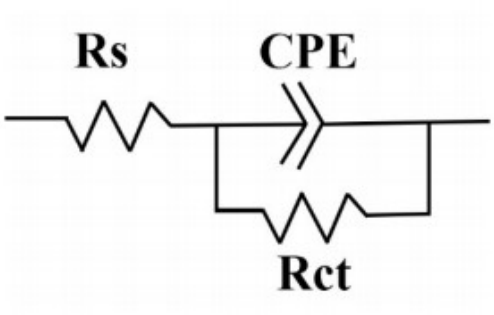

Figure S19. The equivalent circuits of OER.

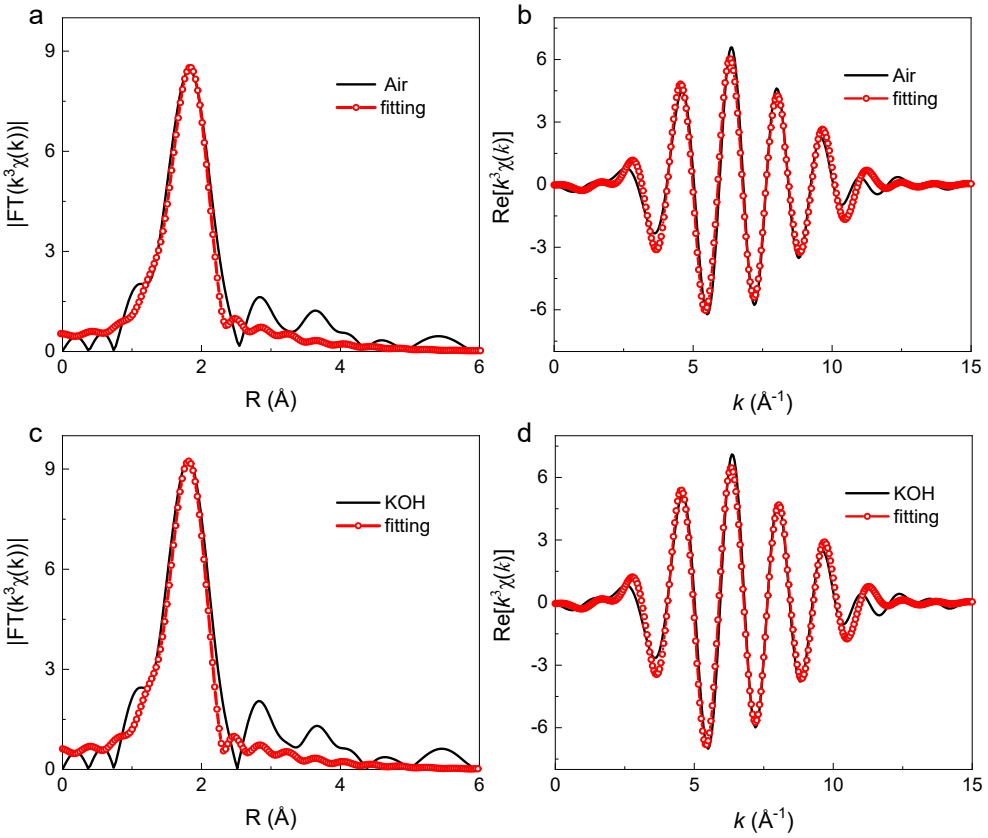

Figure S20. The first-shell fitting of Co *K*-edge EXAFS spectra Fourier transform (FT) spectra under Air (a) and KOH (c) for Mn-$CuCo_2S_4$/NF. The Re[$k^3x(k)$] oscillation and fitting curves under Air (b) and KOH (d).

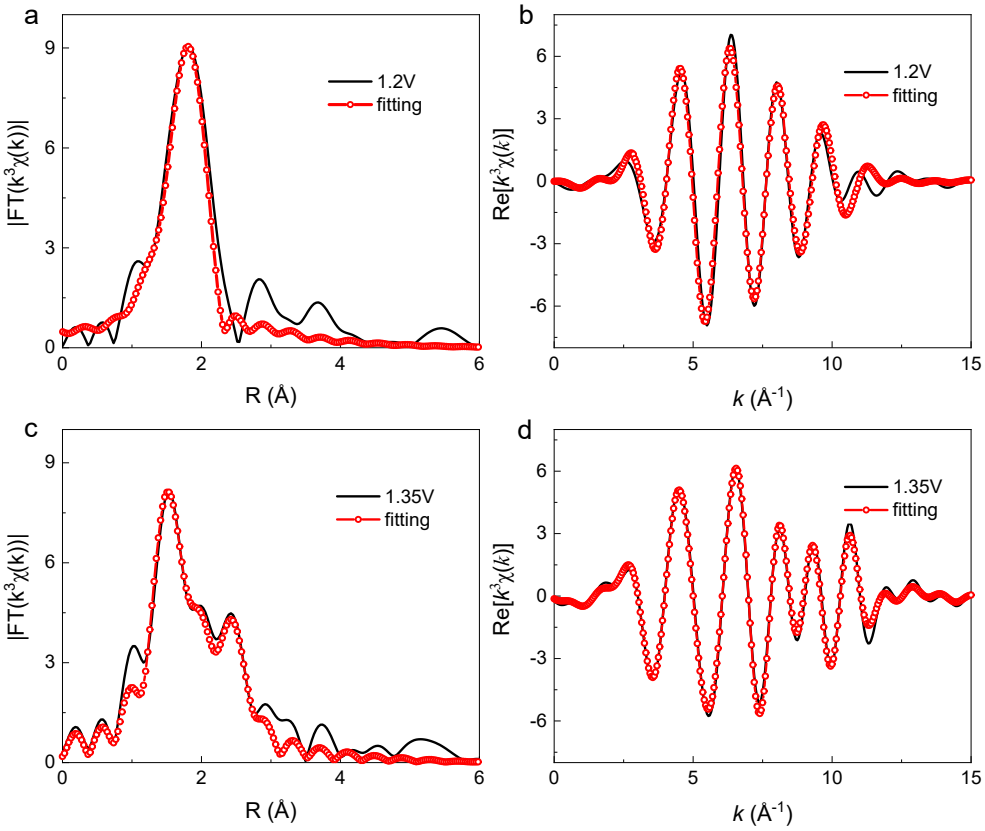

Figure S21. The fitting of Co *K*-edge EXAFS spectra Fourier transform (FT) spectra under 1.2V (a) and 1.35V (c) for Mn-$CuCo_2S_4$/NF. The Re[$k^3x(k)$] oscillation and fitting curves under 1.2V (b) and 1.35V (d).

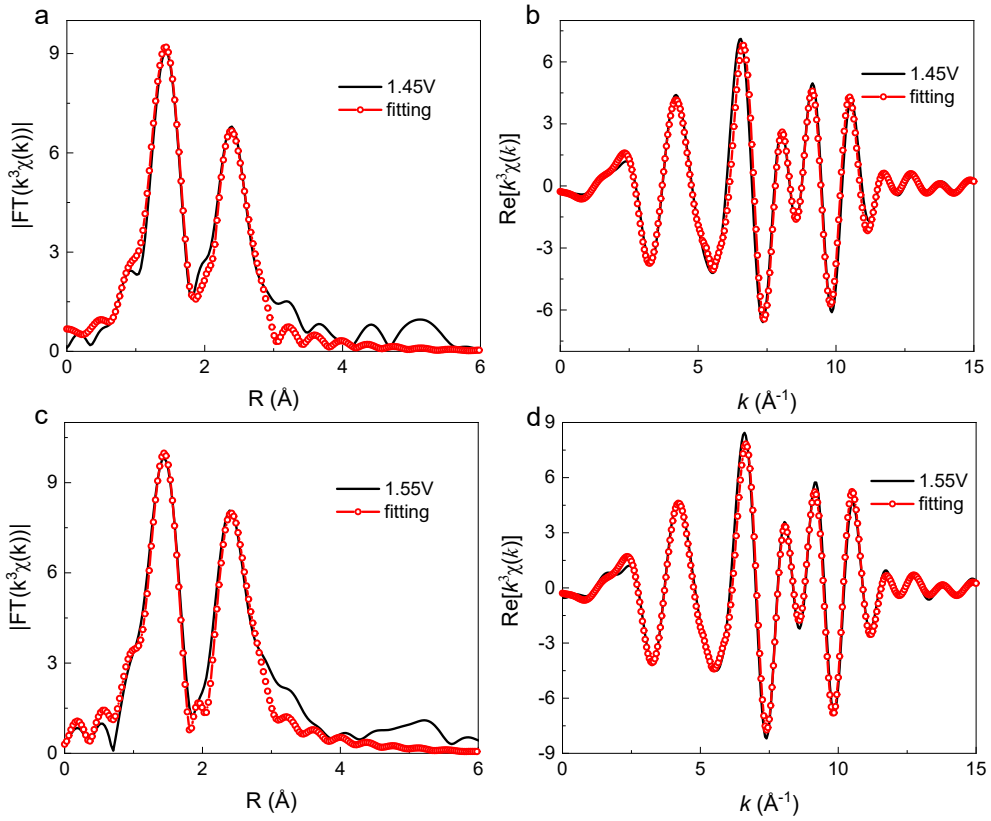

Figure S22. The The fitting of Co *K*-edge EXAFS spectra Fourier transform (FT) spectra under 1.45V (a) and 1.55V (c) for Mn-$CuCo_2S_4$/NF. The Re[$k^3x(k)$] oscillation and fitting curves under 1.45V (b) and 1.55V (d).

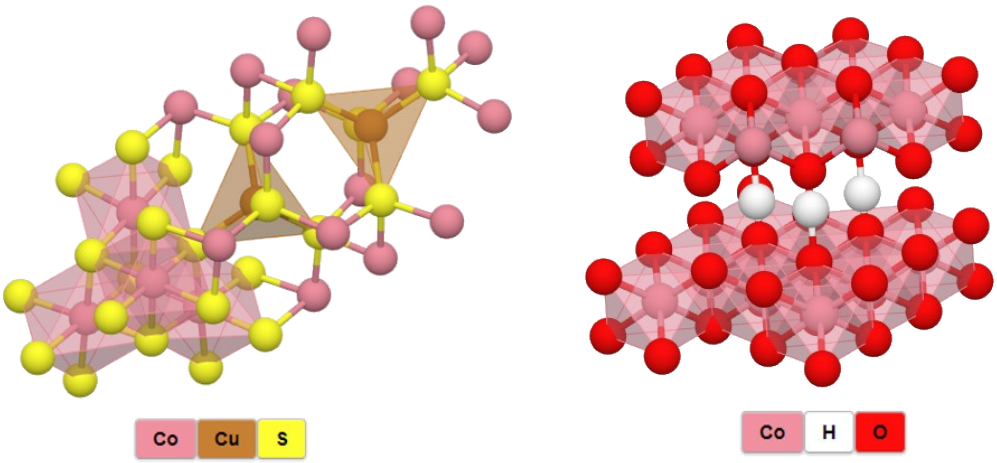

Figure S23. Images of $CuCo_2S_4$ and CoOOH crystal structure

Table S1. ICP-OES results of *v*-M-$CuCo_2S_4$/NF (v-M = Mn, V, and Cr).

Catalysts	Metal (wt %)	Cu (wt %)	Co(wt %)
Mn-$CuCo_2S_4$	3.2	32.45	68.71
Cr-$CuCo_2S_4$	4.31	31.6	70.21
V-$CuCo_2S_4$	3.7	32.89	64.3

Table S2. Comparison of alkaline OER performance for Mn-$CuCo_2S_4$/NF as well as other electrocatalysts reported in the literatures.

Catalysts	Currentdensity ($mA\ cm^{-2}$)	Overpotential (mV)	Electrolyte	Ref.
Mn−$CuCo_2S_4$/NF	1500	378	1MKOH	This work
NiFe LDH/MXene	500	300	1MKOH	1
$NiFe_2O_4$/NiFe LDH	1000	265	1MKOH	2
Sn−Ni_3S_2/NF	1000	580	1MKOH	3
N, Fe-NiSe@NIF	1000	290	1MKOH	4
(Ni−MoO_2)@C/N F	2000	400	1MKOH	5
P-NiCoV-LTH/NF	1000	373	1MKOH	6
CoO_x−RuO_2/NF	1500	420	1MKOH	7
Fe_2P-Co_2P/CF	1000	317	1MKOH	8
Ni_3Fe/FeV_2O_4	1500	350	1MKOH	9
Fe-CoP	1000	428	1MKOH	10

Table S3. The fitted parameters of the EIS data of Mn-$CuCo_2S_4$/NFcatalyst.

Potential (V vs.RHE)	R_s (Ω)	CPE (F)	R_{ct} (Ω)
1.60V	1.623	1.357	0.0248
1.65V	1.632	1.342	0.0222
1.70V	1.630	1.372	0.0248
1.75V	1.631	1.333	0.0230
1.80V	1.633	1.348	0.0192

1

Table S4. Structural parameters extracted from quantitative EXAFS curves-fitting under working condition for Mn-$CuCo_2S_4$/NF using the ARTEMIS module of IFEFFIT.

Samples	Path	N	R (Å)	$\sigma^2(10^{-3}Å^2)$	ΔE_0(eV)	R-factor
Air	Co-S	6.2	2.26	9.2（2.0）	4.75	0.008
KOH	Co-S	6.1	2.25	8.8（1.8）	4.90	0.012
1.20V	Co-S	5.8	2.25	8.5（2.2）	4.53	0.013
1.35V	Co-O	3.16	1.89	5.7	5.3	0.010
	Co-S	1.8	2.28	9.0		
	Co-Co	1.2	2.80	7.1		
1.45V	Co-O	5.1	1.89	6.5	4.7	0.011
	Co-S	0.38	2.28	9.3		
	Co-Co	2.5	2.81	7.2		
1.55V	Co-O	5.6	1.88	6.3	4.4	0.010
	Co-S	0.2	2.49	8.3		
	Co-Co	2.8	2.82	7.5		

References

1 Yu, M. et al. A hierarchically porous and hydrophilic 3D nickel–iron/MXene electrode for accelerating oxygen and hydrogen evolution at high current densities. Nano Energy 63, doi:10.1016/j.nanoen.2019.103880 (2019).

2 Wu, Z., Zou, Z., Huang, J. & Gao, F. NiFe2O4 Nanoparticles/NiFe Layered Double-Hydroxide Nanosheet Heterostructure Array for Efficient Overall Water Splitting at Large Current Densities. ACS Appl Mater Interfaces 10, 26283-26292, doi:10.1021/acsami.8b07835 (2018).

3 Jian, J. et al. Sn-Ni3S2 Ultrathin Nanosheets as Efficient Bifunctional Water-Splitting Catalysts with a Large Current Density and Low Overpotential. ACS Appl Mater Interfaces 10, 40568-40576, doi:10.1021/acsami.8b14603 (2018).

4 Chen, J., Chen, J., Cui, H. & Wang, C. Electronic Structure and Crystalline Phase Dual Modulation via Anion-Cation Co-doping for Boosting Oxygen Evolution with Long-Term Stability Under Large Current Density. ACS Appl Mater Interfaces 11, 34819-34826, doi:10.1021/acsami.9b08060 (2019).

5 Qian, G. et al. Industrially Promising Nanowire Heterostructure Catalyst for Enhancing Overall Water Splitting at Large Current Density. ACS Sustainable Chemistry & Engineering 8, 12063-12071, doi:10.1021/acssuschemeng.0c03263 (2020).

6 Liu, Q. et al. Controllable Conversion from Single-Crystal Nanorods to Polycrystalline Nanosheets of NiCoV-LTH for Oxygen Evolution Reaction at Large Current Density. ACS Sustainable Chemistry & Engineering 8, 16091-16096, doi:10.1021/acssuschemeng.0c06052 (2020).

7 Yu, T. et al. Amorphous CoOx-Decorated Crystalline RuO2 Nanosheets as Bifunctional Catalysts for Boosting Overall Water Splitting at Large Current Density. ACS Sustainable Chemistry & Engineering 8, 17520-17526, doi:10.1021/acssuschemeng.0c06782 (2020).

8 Liu, X. et al. In Situ-Grown Cobalt–Iron Phosphide-Based Integrated Electrode for Long-Term Water Splitting under a Large Current Density at the Industrial Electrolysis Temperature. ACS Sustainable Chemistry & Engineering 8, 17828-17838, doi:10.1021/acssuschemeng.0c06987 (2020).

9 Zhang, H. et al. Interface Engineering of Ni3Fe and FeV2O4 Coupling with Carbon-Coated Mesoporous Nanosheets for Boosting Overall Water Splitting at 1500 mA cm–2. ACS Sustainable Chemistry & Engineering 9, 8249-8256, doi:10.1021/acssuschemeng.1c02293 (2021).

10 Cao, L. M. et al. Fe-CoP Electrocatalyst Derived from a Bimetallic Prussian Blue Analogue for Large-Current-Density Oxygen Evolution and Overall Water Splitting. Adv Sci (Weinh) 5, 1800949, doi:10.1002/advs.201800949 (2018).